Phenomenological model of auditory nerve population responses to cochlear implant stimulation

Tabibi, Sonia ; Boulet, Jason ; Dillier, Norbert ; Bruce, Ian C

Abstract: Background: Models of auditory nerve fiber (ANF) responses to electrical stimulation are helpful to develop advanced coding for cochlear implants (CIs). A phenomenological model of ANF population responses to CI electrical stimulation with a lower computational complexity compared to a biophysical model would be beneficial to evaluate new CI coding strategies. New Method: This study presents a phenomenological model which combines four temporal characteristics of ANFs (refractoriness, facilitation, accommodation and spike rate adaptation) in addition to a spatial spread of the electric field. Results: The model predicts the performances of CI subjects in the melodic contour identification (MCI) experiment. The simulations for the MCI experiment were consistent with CI recipients' experimental outcomes that were not predictable from the electrical stimulation patterns themselves. Comparison with Existing Methods: Previously, no phenomenological population model of ANFs has combined all four aforementioned temporal phenomena. Conclusions: The proposed model would help the further investigations of ANFs responses to different electrical stimulation patterns and comparison of different sound coding strategies in CIs.

DOI: https://doi.org/10.1016/j.jneumeth.2021.109212

Journal of Neuroscience Methods 358 (2021) 109212

Contents lists available at ScienceDirect

Journal of Neuroscience Methods

journal homepage: www.elsevier.com/locate/jneumeth

Phenomenological model of auditory nerve population responses to cochlear implant stimulation

Sonia Tabibi [a,b,c,*], Jason Boulet [d], Norbert Dillier [b,c], Ian C. Bruce [e]

[a] Department of Information Technology and Electrical Engineering, ETH Zurich (ETHZ), Zurich, Switzerland
[b] University Hospital Zurich, Department of Otorhinolaryngology, Head & Neck Surgery, Zurich, Switzerland
[c] University of Zurich, Zurich, Switzerland
[d] Integrative Neuroscience Discovery and Study, McMaster University, Hamilton, ON, Canada
[e] Department of Electrical and Computer Engineering, McMaster University, Hamilton, ON, Canada

ARTICLE INFO

Keywords:
Phenomenological model
Auditory nerve fiber population
Cochlear implant
Spatial spread
Facilitation
Accommodation

ABSTRACT

Background: Models of auditory nerve fiber (ANF) responses to electrical stimulation are helpful to develop advanced coding for cochlear implants (CIs). A phenomenological model of ANF population responses to CI electrical stimulation with a lower computational complexity compared to a biophysical model would be beneficial to evaluate new CI coding strategies.
New method: This study presents a phenomenological model which combines four temporal characteristics of ANFs (refractoriness, facilitation, accommodation and spike rate adaptation) in addition to a spatial spread of the electric field.
Results: The model predicts the performances of CI subjects in the melodic contour identification (MCI) experiment. The simulations for the MCI experiment were consistent with CI recipients' experimental outcomes that were not predictable from the electrical stimulation patterns themselves.
Comparison with existing methods: Previously, no phenomenological population model of ANFs has combined all four aforementioned temporal phenomena.
Conclusions: The proposed model would help the further investigations of ANFs responses to different electrical stimulation patterns and comparison of different sound coding strategies in CIs.

1. Introduction

Cochlear implants (CIs) are successful neural prostheses for severe to profound hearing loss and the number of profoundly hearing-impaired people who have been implanted with a CI is increasing rapidly. However, CI users still have difficulties in realistic listening conditions such as speech presented in competition with noise or other talkers, such as in a cocktail party or a restaurant where background noise is always present (Nie et al., 2005; Wilson et al., 2005). In addition, CI users' performance on tests of tonal languages and melody recognition is still poor (Wilson and Dorman, 2008). These poor performances arise from limited spectral, temporal and amplitude resolutions of CI users compared to normal hearing (NH) listeners. Therefore, many sound coding strategies have been recently proposed to improve a CI users' performance under these demanding situations (Grayden et al., 2004; Nogueira et al., 2005; Laneau et al., 2006; Sit et al., 2007; Vandali and van Hoesel, 2011; Lai et al., 2018). However, evaluation of sound coding strategies needs time consuming clinical experiments which motivates the design and use of models of auditory nerve fiber (ANF) responses to the electrical stimulation to test the predicted neural representation of speech for different sound coding strategies (Seeber and Bruce, 2016; Takanen et al., 2016; van Gendt et al., 2016).

Different types of models of electrically stimulated ANFs exist. Two major categories based on the description of the functionality of the neuron are biophysical models (O'Brien and Rubinstein, 2016) and phenomenological models (Takanen et al., 2016; van Gendt et al., 2016). Phenomenological models have lower computational complexity, and parameters can be more easily adjusted to individual CI recipients. These parameters may have no direct biophysical interpretation, but they may be related to simple stimulus-response characteristics, such as refractoriness. Thus, it may be possible to estimate the individualized parameters using neural response telemetry (NRT) via

* Corresponding author at: Frauenklinikstrasse 24, 8091 Zurich, Switzerland.
E-mail address: sonia.tabibi@usz.ch (S. Tabibi).

https://doi.org/10.1016/j.jneumeth.2021.109212
Received 14 August 2020; Received in revised form 26 April 2021; Accepted 29 April 2021
Available online 3 May 2021

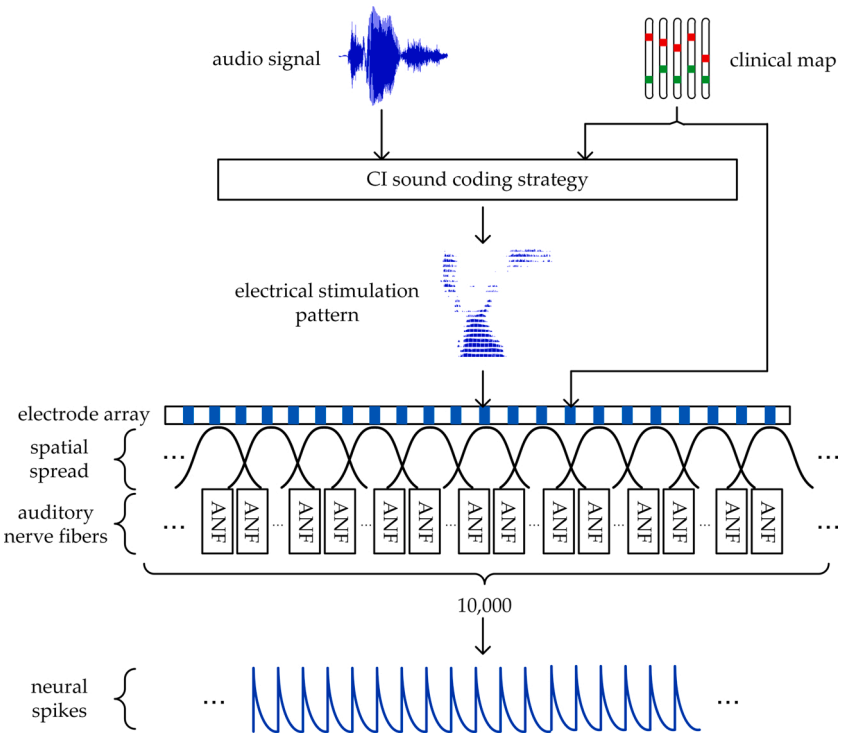

Fig. 1. Sketch of phenomenological model of ANFs responses to the electrical stimulation. The model includes the CI stimulation pattern and the patient's clinical map as inputs and auditory nerves spikes as an output. ANF blocks contain refractoriness, facilitation, accommodation and SRA as temporal dynamics. The number of auditory nerve fibers in the model is 10,000.

measuring electrically evoked compound action potentials (ECAPs). On the other hand, biophysical models are helpful to understand physiological behavior (O'Brien and Rubinstein, 2016). The computational complexity of biophysical models makes these models less efficient for comparison of different CI sound coding strategies, although these models can simulate the ANFs response to the electrical stimulation very well (Hodgkin and Huxley, 1952; Rattay, 1999; Mino et al., 2004; Imennov and Rubinstein, 2009). Thus, a phenomenological model of a neural population in response to the electrical stimulation was developed in this study.

Dependency of the auditory nerve response on spiking and stimulus history has been reported in many studies (Dynes, 1996; Bruce et al., 1999a; Cartee, 2000; Miller et al., 2008; Cohen, 2009c; Boulet et al., 2016; Hughes and Laurello, 2017). As reviewed by Boulet et al. (2016), this dependency can be defined in the form of refractoriness, facilitation, accommodation and spike rate adaptation (SRA). Refractoriness and SRA are spike-dependent phenomena and facilitation and accommodation are subthreshold stimulus-dependent phenomena. Refractoriness is defined as a reduction in the excitability of ANFs immediately following an action potential and has been observed in human CI recipients via measuring the ECAP (Cohen, 2009c; Botros and Psarros, 2010). Facilitation (also referred to as temporal summation) is an increase in a nerve excitability caused by subthreshold stimulation in short intervals and was reported in animal studies (Dynes, 1996; Cartee, 2000; Heffer et al., 2010) and human CI recipients (Cohen, 2009c; Karg et al., 2013; Hey et al., 2017; Tabibi et al., 2019). ANFs display a gradual drop in their spiking probability in response to an ongoing pulse train, which is defined as SRA. Animal experiments (Nourski et al., 2006; Zhang et al., 2007; Miller et al., 2008) in addition to ECAP measurements of human CI users (Lai and Dillier, 2009; Zhang et al., 2013; Hughes and Laurello, 2017) have shown traces of SRA as decrements in the neural excitability. In parallel to SRA, accommodation (also referred to as subthreshold adaptation) can reduce excitability for the current pulse when there is a subthreshold response to the previous pulse (i.e. no spike) and the interval between two pulses is large enough to allow the membrane potential to decay back near or below the resting potential (Dynes, 1996; Boulet et al., 2016).

In addition to all the aforementioned temporal phenomena, there are also spatial interactions or spread of the electrical stimulation current that may reduce the information provided on the individual electrodes and decrease the selectivity and number of effective electrodes in CIs (Abbas et al., 2004; Undurraga et al., 2012). The electrical spread is measurable via NRT and the standard 'forward-masking' paradigm for artifact cancellation technique (Lai and Dillier, 2000; Lai et al., 2002; Cohen et al., 2003). Studies have shown that the stimulus level has an effect on the shape of the excitation profile; the increase of the stimulus strength increases the amplitude of the profile. The Cohen et al. (2004) study did not reveal a significant effect of stimulus level on the width (distance along the electrode array from the stimulated electrode to the interacted electrodes) of the neural excitation profile. In contrast, other studies reported that the increase in the level not only increases the amplitude of the profile but also broadens it (Abbas et al., 2004; Cohen, 2009b; Hughes and Stille, 2010).

In this study, a phenomenological model of single-fiber response to electrical stimulation was used and the model was extended to a population of ANFs. The extension was made to enable comparison of different sound coding strategies for individual CI recipients. For this purpose, a CI subject's clinical map and an electrical stimulation pattern generated with a specific sound coding strategy were used as inputs for the model. Boulet (2016)'s model was used because no phenomenological model has combined all four aforementioned temporal phenomena (refractoriness, facilitation, SRA and accommodation) and the model is computationally efficient compared to biophysical models. In addition to all these temporal phenomena, the symmetric simplified profile of the spatial spread of the electric field was modeled. Finally, the auditory neural time-frequency representation generated by the model was compared to the one generated by the auditory periphery model (Zilany et al., 2009, 2014) by means of a similarity index measure (Hines and Harte, 2010, 2012). Thus, this study focuses on the extended model of Boulet (2016) and how efficient this model could be in the

comparison of different sound coding strategies for individual CI subjects.

2. Materials and methods

2.1. General structure of the model

The general structure of the model is shown in Fig. 1 with 10,000 neurons for auditory nerve cells. An acoustic signal was processed with a sound coding strategy and the generated electrical stimulation pattern, together with a CI patient's clinical map used to generate the electrical pulses, were used as inputs to the model. Thus, the number of active electrodes, stimulation rate, threshold (T) levels, comfort (C) levels, phase width and interphase gap would be different for individual CI recipients. Then, the output of different electrodes was spread over the population of neurons adjacent to that electrode whereby the spatial spread was broadened with increasing stimulus level (Abbas et al., 2004; Cohen, 2009b; Hughes and Stille, 2010). It is worth mentioning that the model was restricted to the clinically used biphasic pulses and only the cathodic phase of the pulses was modeled (Fredelake and Hohmann, 2012; Jeng et al., 2009).

The extracellular current from the CI stimulation strategy was scaled to account for the fraction of the current delivered by a scala tympani electrode array that actually leads to depolarization of ANFs. Since T levels are not the same for different CI subjects, the amount of extracellular current varies. Thus, the scaling factor was individualized based on extracellular threshold current of CI recipients on different electrodes. In order to individualize the scaling factor, the threshold current for each electrode was extracted from the CI recipient's clinical map. This value is specified on the current level (CL) which can be converted to mA according to Eq. (1) (Irwin, 2006).

$$I = 17.5 \times 100^{CL/255} \times 10^{-3} \quad (\text{mA}) \tag{1}$$

In cats it was shown that the mean threshold current for a 26 μs extracellular cathodic stimulus is 0.90 mA with 2.99 dB standard deviation (SD) (Miller et al., 1999) and a single pulse intracellular threshold current with the same phase width is approximately 91 pA according to the model of Boulet (2016). Extracellular threshold currents for different electrodes from a patient's clinical map were converted from CL to mA with Eq. (1) and then their standard deviations in dB ($SDex_i$) were computed with Eq. (2); where index i is the electrode number and $TLevel_i$ is the extracellular threshold current in mA for that electrode.

$$SDex_i = \frac{TLevel_i \times 2.99}{0.9} \quad (\text{dB}) \tag{2}$$

Then, a uniform distribution of extracellular threshold currents ($TLevel_i$) with $SDex_i$ standard deviation was considered and the scaling factor was defined as a division of the distribution of $TLevel_i$ and the intracellular threshold current (91 pA). Finally, in order to calculate the intracellular currents which were injected to the model, the extracellular currents from CI stimulation were divided by the computed scaling factors.

The total number of electrodes in the Nucleus devices from Cochlear® is 22 and 3 extra ANF sub-populations in the apex were considered in this model to investigate the effect of spatial spread of the electric field. The numbering of the neural sub-populations was based on the number of the closest electrode (1–22) or extrapolated electrode position (23–25). The model temporal and spatial phenomena description provided in Sections 2.2–2.5.

2.2. Refractoriness

One of the prominent temporal characteristics of ANFs in response to the electrical stimulation is refractoriness. Refractoriness is defined as a decrease in neural excitability because of a spike in response to the previous stimulation. The refractory period can be divided into an absolute refractory period (ARP) during which the auditory nerve is incapable of responding to the following pulse and a relative refractory period (RRP) during which a greater stimulus intensity is needed to cause a response compared to the interval when the neuron is outside the refractory period (Bruce et al., 1999a; Boulet et al., 2016). The primary biophysical mechanisms that lead to refractoriness are the inactivation of sodium (Na) channels and the activation of delay-rectifier potassium (K) channels (Hodgkin and Huxley, 1952), but the dynamics of other voltage-gated ion channels can also influence the absolute and relative refractory periods (e.g., Negm and Bruce, 2014; Boulet and Bruce, 2017). Refractoriness can impose limitations on the maximum effective stimulation rate of CIs since ANFs cannot respond to a stimulus presented during the ARP. Effects of refractoriness on threshold and RS were reported by Miller et al. (2001) and can be written as Eqs. (3) and (4) where $\tau_{\theta,r}$ is a relative refractory period for threshold, $\tau_{RS,r}$ is a relative spread time constant for refractoriness and t_{abs} is an absolute refractory period.

$$R_\theta = \begin{cases} \infty & \text{if} \quad t < t_{abs} \\ \dfrac{1}{1 - \exp(-\dfrac{t - t_{abs}}{\tau_{\theta,r}})} & \text{otherwise} \end{cases} \tag{3}$$

$$R_{RS} = 1 + \exp(-\frac{t - t_{abs}}{\tau_{RS,r}}) \tag{4}$$

2.3. Facilitation and accommodation

As mentioned earlier, facilitation and accommodation are subthreshold stimulus-dependent phenomena. Following a subthreshold response to the previous stimuli, the neural excitability to the next pulse can either increase (facilitation) or decrease (accommodation). Facilitation for a biphasic stimulation relates to sodium activation near threshold. When the membrane potential is near the threshold potential and the neuron does not produce an action potential, residual sodium activation can increase the excitability to the next pulse. But sodium channel inactivation limits the duration over which facilitation can accumulate (Boulet et al., 2016). Traces of facilitation were reported in animal studies (Dynes, 1996; Cartee, 2000; Heffer et al., 2010), and recently ECAP measurements have been recorded for a facilitation effect in human CI recipients (Hey et al., 2017; Tabibi et al., 2019). In the current study the effects of facilitation on threshold and RS were defined from the study by Dynes (1996). Thus, the same function with different coefficients and time constants was applied for facilitation effects on threshold and RS (Eq. (5)) where $\tau_{\theta,f}$ is a threshold time constant for facilitation, $\tau_{RS,f}$ is a relative spread time constant for facilitation, $a_{\theta,f}$ is a threshold strength for facilitation and $a_{RS,f}$ is a relative spread strength for facilitation. There is no facilitation effect when the time since last spike (t_{sp}) or the pulse offset time (t_{off}) are zero. Facilitation was reset at every pulse offset time to approximate the effect of sodium inactivation on facilitation (Boulet, 2016).

$$F_{\theta,RS} = \begin{cases} 0 & \text{if} \quad t_{sp} = 0 \quad \text{or} \quad t_{off} = 0 \\ a_{\theta,f/RS,f} \times \exp(-\dfrac{t}{\tau_{\theta,f/RS,f}}) & \text{otherwise} \end{cases} \tag{5}$$

It has been suggested that hyperpolarization-activated cyclic nucleotide-gated (HCN) channels in ANFs may be responsible for producing accommodation (subthreshold adaptation) (Negm and Bruce, 2014; Boulet and Bruce, 2017). If a subthreshold stimulus is followed by a new stimulus after a relatively large delay, the membrane potential drops below the resting potential and the threshold for the current stimulus increases which leads to reduced excitability for the stimulus. Two components were considered for the accommodation effect; a 'slow' accommodation component extracted from biophysical model studies (Negm and Bruce, 2014; Boulet and Bruce, 2017) and a 'quick'

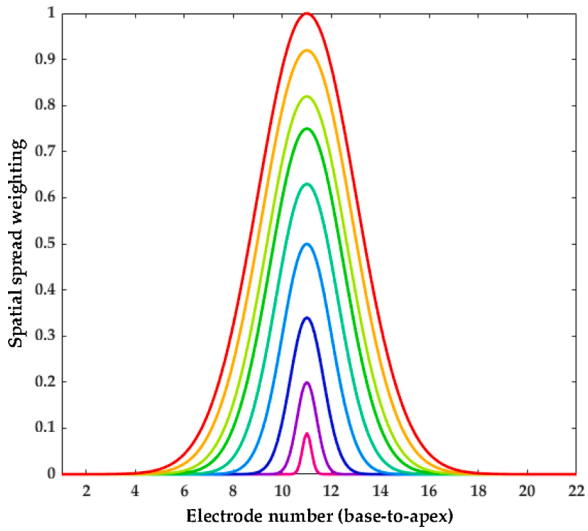

Fig. 2. Example spatial spread profiles of 9 different stimulus intensities with a stimulation presented on electrode 11. An electrical stimulus with the highest strength produces the profile with the highest weighting and broadest width. The x-axis represents the electrode number in basal-to-apical order and spatial spread weighting in a range of 0–1 is shown on the y-axis.

accommodation component from the study by Dynes (1996) and also described by biophysical model of Boulet and Bruce (2017). Each of the accommodation components can be defined according to Eq. (6) where $\tau_{\theta,a}$ is a threshold time constant for accommodation, $\tau_{RS,a}$ is a relative spread time constant for accommodation, $a_{\theta,a}$ is a threshold strength for accommodation and $a_{RS,a}$ is a relative spread strength for accommodation. The final accommodation effect was defined as a summation of 'slow' and 'quick' components. Accommodation accumulates over sequential non-spiking responses as opposed to facilitation (Negm and Bruce, 2014) and therefore has a longer time constant than facilitation (50 ms compared to 0.5 ms).

$$A_{\theta,RS} = a_{\theta,a/RS,a} \times \exp(-\frac{t}{\tau_{\theta,a/RS,a}}) \quad (6)$$

2.4. Spike rate adaptation (SRA)

The stimuli that CI recipients listen to in their daily life are modulated pulse trains which encourages us to investigate the responses of ANFs to pulse trains at different stimulation rates. It was shown that in human CI subjects, the adaptation pattern is observable for the rates in the range of 400–2400 pps (Hughes et al., 2012). Adaptation is defined in animal studies (Nourski et al., 2006; Zhang et al., 2007; Miller et al., 2008) as decrements in neural excitability beyond what can be explained by refractoriness (Boulet et al., 2016). In ECAP measurements, adaptation can be seen as an overall reduction in ECAP amplitude relative to the amplitude for the first pulse (Hughes et al., 2012; Hughes and Laurello, 2017). It was shown in Negm and Bruce (2014) and Boulet and Bruce (2017) that low-threshold potassium (KLT) and HCN channels may be responsible for adaptation. However, adaptation at higher stimulation rates is due to KLT channels, whereas the adaptation due to HCN channels is observed across all stimulation rates (Negm and Bruce, 2014). SRA in our phenomenological model is from the Nourski et al. (2006) study in which the initial value of adaptation was set to 1. In contrast to the Nourski et al. (2006) study, the effect of SRA on the threshold in this study was incremented by a fractional quantity $\rho_{\theta,s/RS,s}$ which reduced the excitability of the ANF (Boulet, 2016).

$$SRA_{\theta,RS}(t) = SRA(t - \Delta t)_{\theta,RS} + \rho_{\theta,s/RS,s} \quad (7)$$

Then the recovery of adaptation occurred over the timescale $\tau_{\theta,s/RS,s}$ by a linear differential equation as is shown in Eq. (8);

$$\frac{dSRA_{\theta,RS}}{dt} = \frac{1}{\tau_{\theta,s/RS,s}}[1 - SRA_{\theta,RS}(t)] \quad (8)$$

The effect of SRA on the relative spread is unknown, thus the effects of SRA on RS were modeled with the same equations as the threshold. It is worth noting, however, that the adaptation time constant ($\tau_{\theta,s/RS,s}$) and the spike-dependent increment ($\rho_{\theta,s/RS,s}$) parameters were set to different values from the Nourski et al. study as our model parameters were based on a larger selection of published ANF recordings.

2.5. Spatial spread

Electrical stimulation from a CI electrode produces an electric field which spreads out within the cochlea and excites not only ANFs close to the stimulated electrode but also ANF populations on the neighboring electrodes. However, it was shown that a peak of the response is at or near the stimulated electrode with a decrement towards neighboring electrodes (Abbas et al., 2004; Cohen, 2009b; Hughes and Stille, 2010). Thus, the spatial spread function can be considered as a set of weights centered on the stimulated electrode, with the central weight being the largest (the largest weight was set to 1). In this study, this function was assumed to be symmetric and an example is shown in Fig. 2 in which the highest stimulus intensity has the highest weighting and the broadest width (bigger standard deviation for a Gaussian function). In this figure the stimulation is presented on electrode 11 therefore, the means of the Gaussian functions were set to 11 and the standard deviations were weighted by the stimulus intensities; higher stimulus intensities make the standard deviations bigger. The electrode number in basal-to-apical order (1–22) is shown on the x-axis while the y-axis represents spatial spread weighting normalized to 1.

2.6. Simulation time

Simulation time steps for 10,000 neurons were set to 1 μs in order to capture all the dynamics of the membrane and threshold responses correctly. For instance, for an input audio signal with 1 second length, each of the auditory nerve fiber is simulated for 1,000,000 time steps. To reduce the simulation running time, the simulation was performed with parallel computing in MATLAB R2016b on the Euler (Erweiterbarer, Umweltfreundlicher, Leistungsfaehiger ETH-Rechner) cluster at ETH Zurich.

2.7. Validation

The model outcomes were validated by melodic contour identification (MCI) experiment results conducted with the implementation of a Gammatone filterbank within the CI sound processor algorithm in an earlier study (Tabibi et al., 2017). In addition, the neurogram similarity (NSIM) index measure was used for the comparison of the model output with the auditory periphery model (Zilany et al., 2009, 2014).

2.7.1. Melodic contour identification (MCI)

In the MCI experiment (Galvin et al., 2007) 5 different patterns with 3 tones in each pattern were tested with either the standard fast Fourier transform (FFT) or the Gammatone filterbanks and the musical interval between successive tones in each pattern was varied from 1 to 3 semitones. In general CI recipients performances were better with the Gammatone filterbank than the standard FFT filterbank and a statistically significant effect of the Gammatone filterbank was found for the 1-semitone interval between successive notes (Tabibi et al., 2017). Furthermore, results of the experiment for each CI subject per pattern, per interval and per filterbank were investigated.

Among the 5 aforementioned melodic contour patterns in the MCI experiment, the 'Fall-Rise' and the 'Rise-Fall' patterns were the most difficult patterns for CI recipients to distinguish (Tabibi et al., 2017);

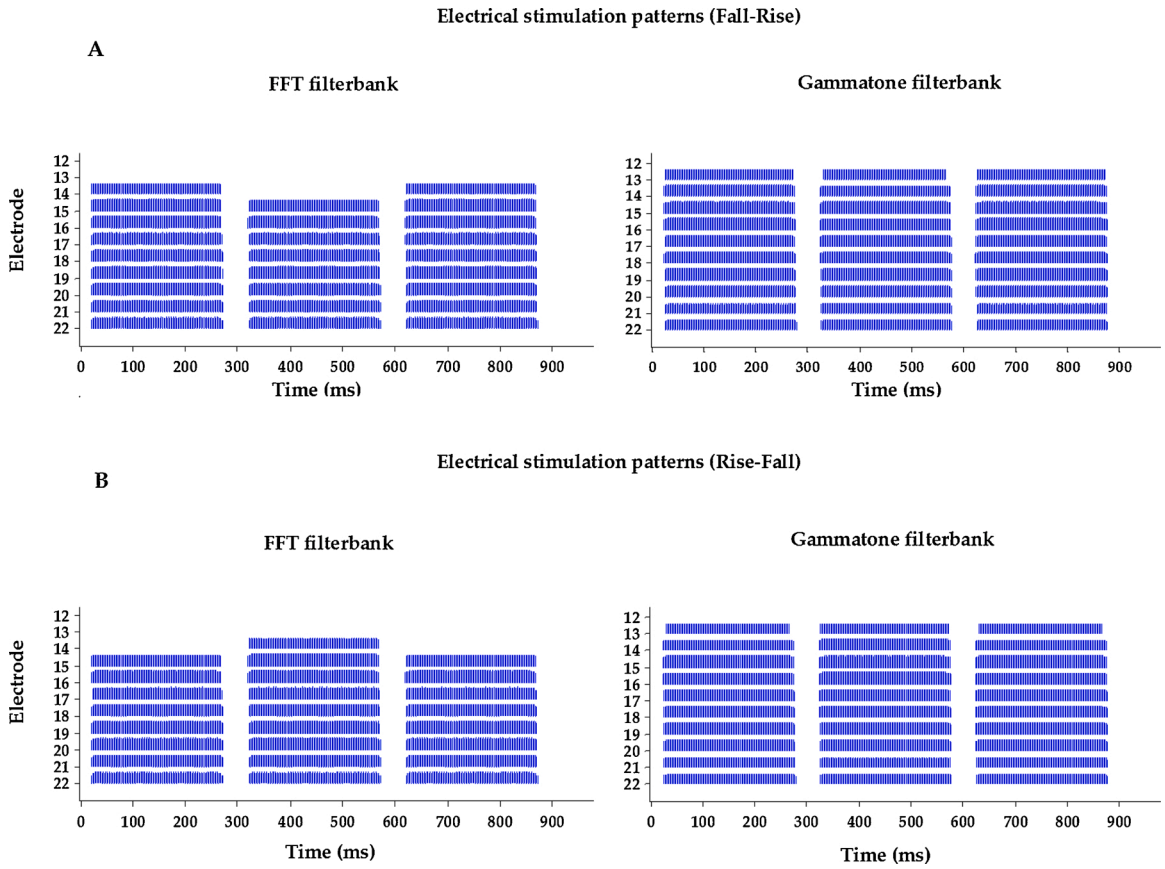

Fig. 3. Example electrodograms for (A) the 'Fall-Rise' and (B) the 'Rise-Fall' patterns with 2-semitone interval from the MCI experiment. The figure shows the electrical stimulation patterns obtained with the standard FFT (first column) and the Gammatone filterbanks (second column) from subject S5. Time in ms is shown on the x-axis while electrode numbers in apical-to-basal order are shown on y-axis.

therefore these 2 patterns were selected for an additional analysis and case study. There were some cases where the electrical stimulation patterns (electrodograms) indicated possible benefits of one filterbank over the other one (the MCI pattern was distinguishable in the electrodogram), but the subject performance did not reveal these benefits. This is shown in Figs. 3 and 4 for two CI recipients (S5 and S7) who participated in the Tabibi et al. (2017) study for the comparison of the standard FFT filterbank with the Gammatone filterbank. The x-axis displays time in milliseconds (ms) and the y-axis electrode numbers in apical-to-basal order. The electrodograms are truncated to the range of active electrodes (22–12).

Fig. 3 represents the electrodograms of subject S5 with the standard FFT filterbank (left) and the Gammatone filterbank (right) for the 'Fall-Rise' pattern (upper row, Fig. 3A) and the 'Rise-Fall' pattern (lower row, Fig. 3B) with the 2-semitone interval. The performance of this subject for the 'Fall-Rise' pattern was 80% correct responses for the Gammatone filterbank whereas the percentage correct responses for the standard FFT filterbank was only 30%. The electrical stimulation pattern for the Gammatone filterbank looks more like the 'Flat' pattern in contrast to the electrodogram of the standard FFT filterbank which shows a clear 'Fall-Rise' pattern. The performance of the subject for the 'Rise-Fall' pattern was 20% correct responses for the standard FFT filterbank and 30% correct responses for the Gammatone filterbank although the electrodogram for the Gammatone filterbank resembles the 'Flat' pattern and the standard FFT filterbank electrodogram shows a clear 'Rise-Fall' pattern.

Fig. 4 represents the electrodograms of subject S7 with the standard FFT filterbank (left) and the Gammatone filterbank (right) for the 'Fall-Rise' pattern (upper row, Fig. 4A) and the 'Rise-Fall' pattern (lower row, Fig. 4B) with the 2-semitone interval. The performance of this subject for the 'Fall-Rise' pattern was 50% correct responses for the standard FFT filterbank whereas the percentage correct responses for the Gammatone filterbank was 90%. This result could be predicted from the electrodograms and therefore, will be used to check whether the model is capable of predicting the test results in the same way as electrodograms. However, the performance of the subject for the 'Rise-Fall' pattern with the standard FFT filterbank was not predictable from the electrodogram, since the contour of the electrodogram was very flat, but the performance was 90% correct responses. The performance of S7 for the 'Rise-Fall' pattern with the Gammatone filterbank was 100% correct.

As these examples show, the electrodogram may be helpful to visualize stimulation patterns, but it does not seem to be a reliable tool to predict the performance of CI recipients in the MCI experiment and the experimental outcome could not always be predicted on the basis of the electrodogram patterns. Therefore, it seems worthwhile to investigate whether the phenomenological model of ANFs responses to the electrical stimulation can provide better predictions of CI subjects' performances.

2.7.2. Acoustic stimulation auditory periphery model

The auditory periphery model of Zilany et al. (2009, 2014) can produce ANF responses to the acoustic stimulation and characterizes the auditory pathway from the middle ear to the auditory nerve. This model can be used as a reference model in this study and a specific audio signal (e.g. a melodic contour pattern) was presented as an input to the model. The output of the model was an auditory neural time-frequency representation which is referred as the 'neurogram' (Bruce, 2017). For every input signal, the auditory periphery model was used to compute a set of auditory nerve post-stimulus time histograms (PSTHs) at 25 characteristic frequencies (CFs) equivalent to the Greenwood frequency position (Greenwood, 1990) of 25 ANF sub-populations in the phenomenological

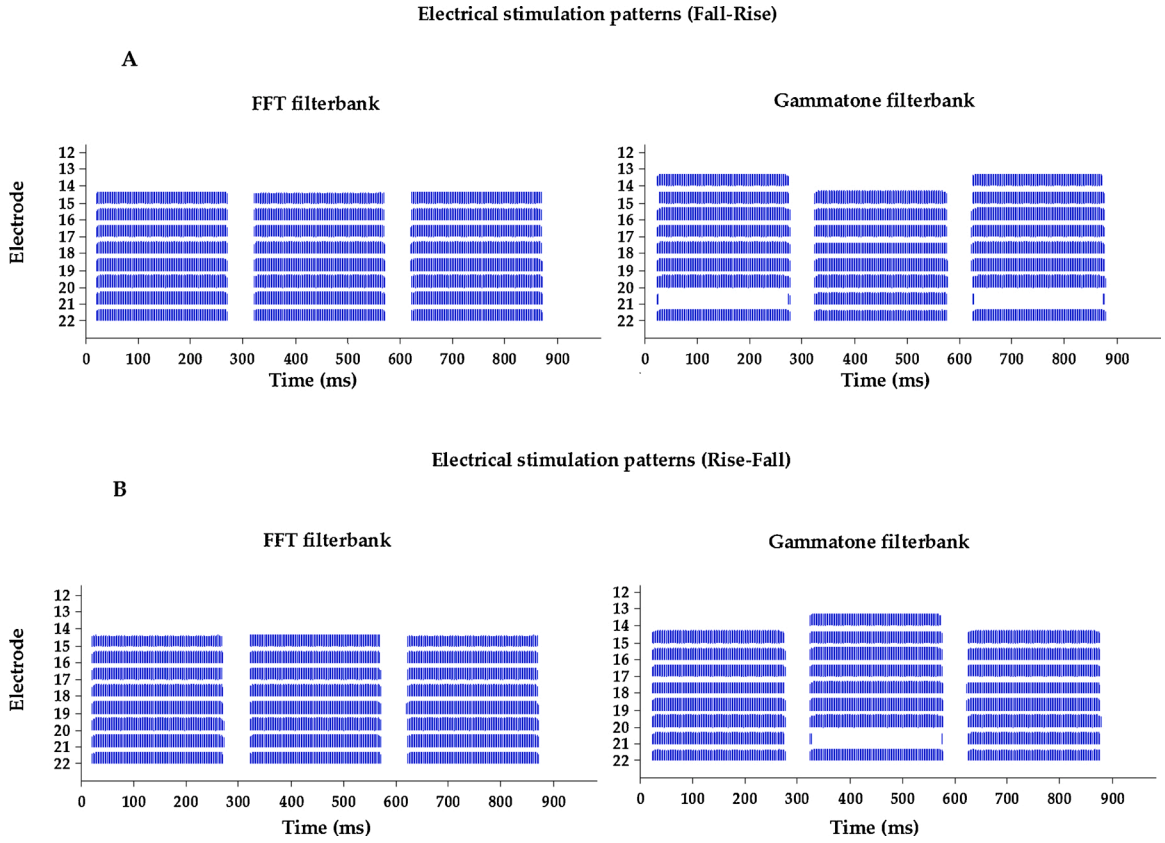

Fig. 4. Example electrodograms for (A) the 'Fall-Rise' and (B) the 'Rise-Fall' patterns with 2-semitone interval from the MCI experiment. The figure shows the electrical stimulation patterns obtained with the standard FFT (first column) and the Gammatone filterbanks (second column) from subject S7. Time in ms is shown on the x-axis while electrode numbers in apical-to-basal order are shown on y-axis.

electrical model. A set of 400 ANFs for each CF was considered with the following composition: 240 high spontaneous-rate (>18 spikes per second) fibers, 80 medium spontaneous-rate (0.5–18 spikes per second) fibers and 80 low spontaneous-rate (<0.5 spikes per second) fibers (Wirtzfeld et al., 2017a,b). The sampling rate of the auditory periphery model was set to 100 kHz. Each raw neurogram was processed to produce mean-rate and fine-timing neurograms. A mean-rate neurogram was constructed from a raw neurogram by rebinning it to 100 μs time bins and convolving with a 128-sample Hamming window at 50% overlap. The fine-timing neurogram was constructed by rebinning to 10 μs time bin and then convolving with a 32-sample Hamming window at 50% overlap (Wirtzfeld et al., 2017a).

The NSIM index measure was used in this study to compare the neurograms generated by the auditory periphery model with the neurograms generated by the phenomenological electrical model. The NSIM index was developed by Hines and Harte (2010, 2012) which was used in this study to quantify informational cues in mean-rate and fine-timing neurograms using an image quality assessment model (Wang et al., 2004). To calculate the NSIM, a 3-by-3 kernel was moved across the neurogram and a local NSIM value was calculated at each position and then the overall NSIM value was computed by averaging the calculated local NSIM values. Three properties were used in the NSIM calculation; 'luminance' (μ_R and μ_D), 'contrast' (σ_R and σ_D) and 'structure' (σ_{RD}) where R subscript refers to the 'reference' neurogram (neurogram generated from the auditory periphery model of Zilany et al. (2009, 2014)) and D subscript refers to the 'degraded' neurogram (neurogram generated from the phenomenological electrical model). 'Luminance' corresponds to the spike rate, 'contrast' measures the standard deviation of spike rates and 'structure' measures the correlation in firing rate between the two neurograms (Wirtzfeld et al., 2017b). The NSIM index is presented in Eq. (9) and weighting parameters (α, β, γ) in this index were set to (1, 0, 1) respectively (Hines and Harte, 2012). The regularization coefficients had different values compared to what was used in Hines and Harte (2010, 2012) study and were set to $C_1 = 6.5025$ and $C_2 = C_3 = 162.5625$ (Wirtzfeld et al., 2017b).

$$\mathrm{NSIM}(R,D) = \left(\frac{2\mu_R\mu_D + C_1}{\mu_R^2 + \mu_D^2 + C_1}\right)^{\alpha} \cdot \left(\frac{2\sigma_R\sigma_D + C_2}{\sigma_R^2 + \sigma_D^2 + C_2}\right)^{\beta} \cdot \left(\frac{\sigma_{\mathrm{RD}} + C_3}{\sigma_R\sigma_D + C_3}\right)^{\gamma} \quad (9)$$

Two methods of scaling the neurograms were used in this study: the Hines and Harte (2010, 2012) method and the Wirtzfeld et al. (2017a,b) method. In the Hines and Harte (2010, 2012) methodology, the mean-rate and fine-timing neurograms were scaled so that the maximum neurogram value, in the units of raw spike count or spikes per second, was scaled to 255 and the remaining values were scaled to the range [0, 255]. Therefore, the spike pattern is more important than the actual spike rate in the Hines and Harte (2010, 2012) scaling method. An alternative scaling method was proposed by Wirtzfeld et al. (2017a,b) which reflected physiological and psychoacoustic data and improved predictions of speech intelligibility. In this method, the neurograms were scaled in units of spikes per second averaged over 400 ANFs per CF compared to the scaling of [0, 255] and therefore, the overall discharge rate matters in addition to the spike pattern.

It is worth mentioning that the average mean-rate NSIM values with the Hines and Harte (2010, 2012) scaling method were estimated by Wirtzfeld et al. (2017a) to have a lower bound of 0.26 and an upper bound of 0.57. The average mean-rate NSIM values with the Wirtzfeld et al. (2017a,b) scaling method were found to have a lower bound of 0.0090 and an upper bound of 0.41. The lower and upper bounds for the average fine-timing NSIM values are 0.25 and 0.56 for the Hines and Harte (2010, 2012) and 0.069 and 0.35 for the Wirtzfeld et al. (2017a,b) scaling methods according to the estimates of Wirtzfeld et al. (2017a).

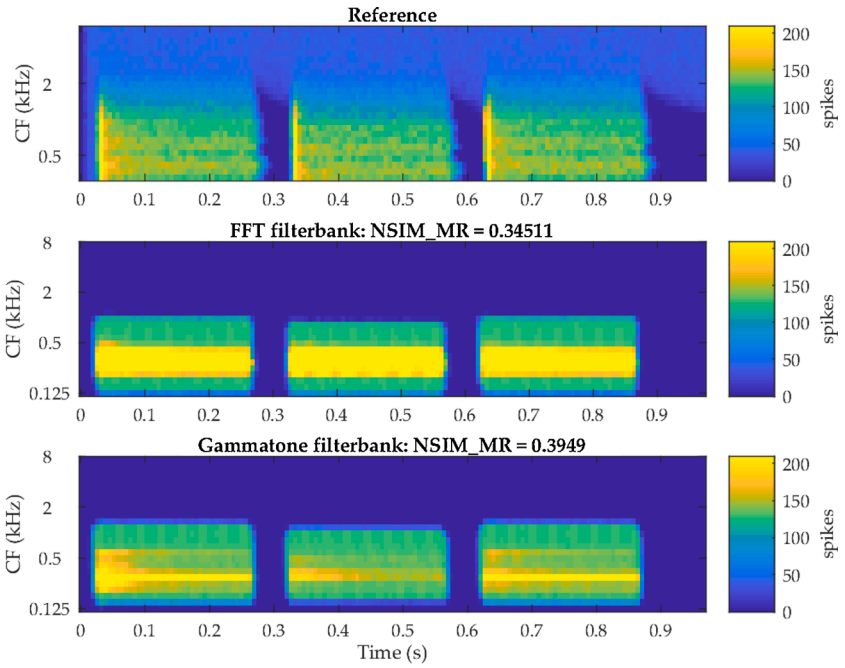

Fig. 5. Mean-rate neurograms of the 'Fall-Rise' pattern with 2-semitone interval and the Hines and Harte (2010, 2012) scaling method presented at 65 dB SPL for subject S5. *Top:* Mean-rate neurogram from the Zilany et al. (2009, 2014) periphery model. *Middle:* Mean-rate neurogram from the phenomenological electrical model with the standard FFT frequency allocation. *Bottom:* Mean-rate neurogram from the electrical model with the Gammatone frequency allocations. Time in seconds is shown on the x-axis while characteristic frequencies in kHz are shown on the y-axis.

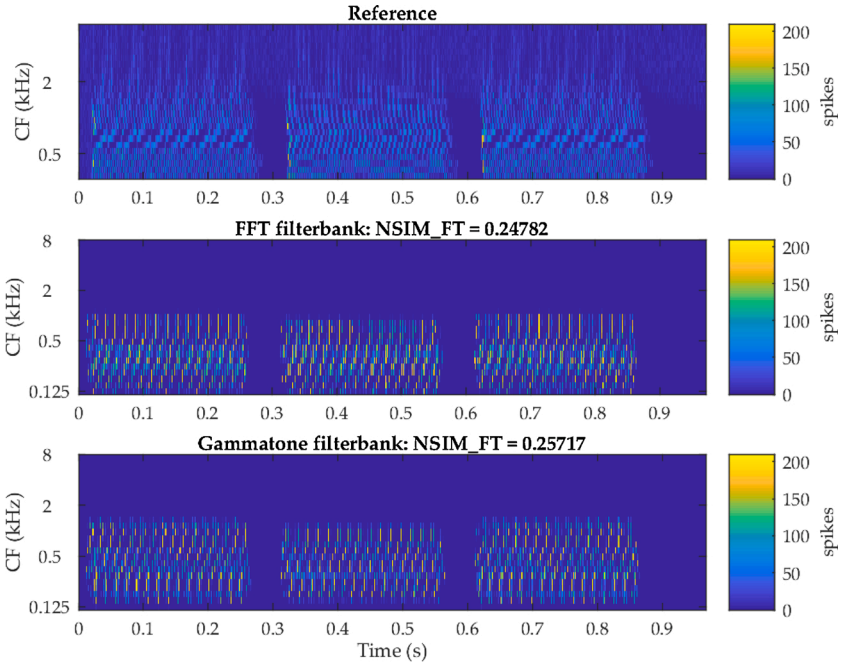

Fig. 6. Fine-timing neurograms of the 'Fall-Rise' pattern with 2-semitone interval and the Hines and Harte (2010) and Hines and Harte (2012) scaling method presented at 65 dB SPL for subject S5. *Top:* Fine-timing neurogram from the Zilany et al. (2009) and Zilany et al. (2014) periphery model. *Middle:* Fine-timing neurogram from the phenomenological electrical model with the standard FFT frequency allocation. *Bottom:* Fine-timing neurogram from the electrical model with the Gammatone frequency allocations. Time in seconds is shown on the x-axis while characteristic frequencies in kHz are shown on the y-axis.

3. Results

NSIM values with the reference to the auditory periphery model of Zilany et al. (2009, 2014) were calculated with 0 indicating no similarity to the auditory periphery model and 1 indicating complete similarity. The electrical stimulation model neurograms were time-shifted to account for the difference in latency between the acoustic model responses and the electrical model responses. Fig. 5 shows the mean-rate neurograms of the 'Fall-Rise' melodic contour pattern of subject S5 with the 2-semitone interval presented at 65 dB SPL. The Hines and Harte (2010, 2012) scaling method was used and the mean-rate neurogram from the Zilany et al. (2009, 2014) periphery model is shown as the reference on top. Fig. 5, middle, is the mean-rate neurogram from the phenomenological electrical model with the standard FFT frequency allocation and Fig. 5, bottom, is the mean-rate neurogram from the electrical model with the Gammatone frequency allocation. NSIM values are written in the figure with the bigger value (0.3949 compared to 0.34511) for the Gammatone filterbank which is consistent with the better performance of subject S5 with the Gammatone filterbank. The x-axis represents time in seconds and the characteristic frequencies in kHz are shown on the y-axis.

In Fig. 5, the 'Fall-Rise' melodic contour pattern is observable in the mean-rate neurogram of the Gammatone filterbank which is in contrast to the electrodogram. In addition, the electrical current leads to the activation of a larger population of ANFs with the FFT filterbank in comparison to the Gammatone filterbank which is an indication of

Table 1
Neurogram similarity index measure for the 'Fall-Rise' and the 'Rise-Fall' patterns of subject S5 with the Hines and Harte (2010, 2012) and the Wirtzfeld et al. (2017a, b) scaling methods. MR represents mean-rate neurogram and FT represents fine-timing neurogram.

	Fall-Rise				Rise-Fall			
	Hines and Harte		Wirtzfeld et al.		Hines and Harte		Wirtzfeld et al.	
	MR	FT	MR	FT	MR	FT	MR	FT
FFT	0.34511	0.24782	0.19585	0.10306	0.33962	0.24635	0.18868	0.09890
Gammatone	0.39490	0.25717	0.23197	0.10355	0.34095	0.25340	0.18704	0.10042

Table 2
Neurogram similarity index measure for the 'Fall-Rise' and the 'Rise-Fall' patterns of subject S7 with the Hines and Harte (2010, 2012) and the Wirtzfeld et al. (2017a, b) scaling methods. MR represents mean-rate neurogram and FT represents fine-timing neurogram.

	Fall-Rise				Rise-Fall			
	Hines and Harte		Wirtzfeld et al.		Hines and Harte		Wirtzfeld et al.	
	MR	FT	MR	FT	MR	FT	MR	FT
FFT	0.31759	0.24027	0.16605	0.10294	0.28896	0.25068	0.15120	0.10429
Gammatone	0.32947	0.25275	0.18124	0.11404	0.28021	0.25161	0.13756	0.10318

larger electric field spread with the FFT filterbank. As it is well known, the electrical current spread has an impact on the number of effective electrodes in CIs (Abbas et al., 1999; Undurraga et al., 2012) and this could explain why the harmonics of the clarinet tones could be better represented with the Gammatone filterbank. As a result, the CI subject had a better performance in the MCI test with the Gammatone filterbank.

Fig. 6 shows the fine-timing neurograms of the 'Fall-Rise' pattern of subject S5 for the reference periphery model (top), the phenomenological electrical model with the FFT frequency allocation (middle) and the phenomenological electrical model with the Gammatone frequency allocation (bottom). The Hines and Harte (2010, 2012) scaling method was used to calculate NSIM values. The Gammatone filterbank had a bigger NSIM value compared to the FFT filterbank which reveals more similarity of the Gammatone filterbank to our reference periphery model. The NSIM values were also calculated for the 'Rise-Fall' pattern and the Wirtzfeld et al. (2017a,b) scaling method for the mean-rate and the fine-timing neurograms and are presented in Table 1. In general, we expected lower NSIM values for the 'Rise-Fall' pattern because the performance of the subject was worse in comparison to the 'Fall-Rise' pattern with both of the filterbanks.

The NSIM values were also calculated for the 'Fall-Rise' and the 'Rise-Fall' patterns of subject S7 and summarized in Table 2. We expected NSIM values of the same range with both filterbanks for the 'Rise-Fall' pattern although the electrodograms looked differently. The NSIM values for the 'Fall-Rise' pattern were higher for the Gammatone filterbank which is consistent with the electrodograms.

4. Discussion

The model described in this study combines temporal characteristics of ANFs in response to the electrical stimulation (refractoriness, facilitation, accommodation and spike rate adaptation) in addition to the spatial spread of the electric field. The model can predict the ANFs responses for individual CI recipients characterized by different clinical maps and sound coding strategies. It accurately simulates neural spikes in response to the electrical stimulation patterns generated with the sound coding strategy. Phenomenological population models that have been developed up to now did not consider all four aforementioned temporal phenomena. For instance, in Fredelake and Hohmann (2012) population model factors such as auditory nerve cell number, spatial spread of the electric field, refractoriness, latency and jitter were investigated. However, the model did not consider peripheral adaptation, accommodation or facilitation. Another example is a population ANF model by van Gendt et al. (2016) where firing threshold was affected by refractoriness, accommodation and spike rate adaptation. However, facilitation was not included in the model. Animal (Dynes, 1996; Cartee, 2000; Heffer et al., 2010) and human (Cohen, 2009c; Karg et al., 2013; Hey et al., 2017; Tabibi et al., 2019, 2020) data has been shown the importance of facilitation in response to the high-rate CI stimulation and consequently models without facilitation would likely produce very different patterns of spiking particularly near the edges of the current spread where the effective current levels are fairly small. Thus, this study is the first to combine all four aforementioned temporal phenomena into a phenomenological model for a population of ANFs.

The model in this study was validated by MCI experiment results from two CI subjects in an earlier study (Tabibi et al., 2017). The procedure of running the model for all 10 CI participants with 2 filterbanks (Gammatone vs. FFT) and 5 melody contour patterns in 3 different semitone intervals is time-consuming and will end up with 300 times of running the model. Therefore, specific cases were selected for the model validation in which there were discrepancies between the electrodogram and CI recipients performance. For these cases, the model simulations were consistent with the participants' experimental outcome which could reveal that electrodogram alone is not always a reliable tool to predict the performance of CI users. However, it could be of interest to run simulations with a bigger sample size in future studies and investigate the consistency between the model outcome and CI recipients' experimental results. Model simulations could also show benefit of one CI coding strategy versus another one, as they could reliably predict the outcome.

The model simulations in this study were run with all forms of temporal interactions; refractoriness, facilitation, spike rate adaptation and accommodation were turned on with their default parameters. However, it would be interesting to investigate how the model outcomes might change if these temporal interactions were turned off or had their parameters changed. It was shown that facilitation has a stronger effect on the CI recipients performance than the other temporal interactions when it is incorporated in the CI coding strategy (Tabibi et al., 2020). Therefore, it would be of interest to run simulations with facilitation turned on/off or with different parameters and explore its influence on model simulations.

In the model presented here the electrode positions in respect to the neural population excited by that electrode was assumed to be equidistant for all electrodes in the intracochlear electrode array. However, the intracochlear electrode type (Straight versus Contour) affects the position of electrodes in the cochlea with smaller distances to the neural interface for perimodiolar versus midscalar or lateral wall electrode

arrays (Tykocinski et al., 2001; Cohen, 2009a). It was shown that the position of the electrode can cause variability in response waveforms and response amplitudes of ECAP (Lai and Dillier, 2000; Lai et al., 2002). It was also reported that electrode position has a significant effect on the spatiotemporal pattern of ANFs responses (Kang et al., 2015). Therefore, it would be interesting to investigate different electrode positions in future studies.

The same distribution of fiber characteristics was considered for all ANFs regardless of their location along the basilar membrane. It was shown that the fiber diameter varies with the position along the basilar membrane (Verveen, 1962; van Gendt et al., 2016) and the variations in ANFs diameters led to differences in adaptation rates (Woo et al., 2010). However, Boulet and Bruce (2017) showed that HCN voltage-gate ion channel heterogeneity may be sufficient to describe differences in ANF adaptation rates, rather than the fiber diameter being a primary factor. Apart from that, a uniform distribution of extracellular threshold currents was considered in the model. The effect of different ANF diameters and extracellular Gaussian distribution need to be investigated in future studies.

The model in this study predicts ANFs responses to the electrical stimulation in CIs. However, most parameters used in the model were acquired from animal studies with different morphology and physiology from human ANFs (Spoendlin and Schrott, 1989; Liu et al., 2015). Thus, it would be interesting to conduct ECAP measurements and optimize the model parameters. The parameters could be individualized for CI recipients (Cohen, 2009c) afterwards because this will help to include the effects of electrode types, electrode positions and fiber characteristics on spatial and temporal components.

The spatial spread function in this study was considered symmetric, although the asymmetry of it has been reported in previous studies (Abbas et al., 2004; Hughes and Abbas, 2006; Cohen, 2009b; van der Beek et al., 2012). However, the asymmetry in spatial spread has not been quantified in details in previous studies and it was not consistent along the electrode array and could be enhanced by limitation of recording methodology (Cohen, 2009b; van der Beek et al., 2012). Therefore, for simplicity the spatial spread function in this study was symmetric and higher stimulus intensities make the profile broader and the amplitude larger (the function was normalized to 1). The simplified version of the spatial spread could be replaced with the estimated profile from ECAP recordings and investigated in future studies.

The number of auditory nerve cells was set to 10,000 neurons as an estimate of the number of surviving ANFs in CI users with a severe to profound hearing loss, consistent with previous studies (Bruce et al., 1999b; Hamacher, 2004; Fredelake and Hohmann, 2012). However, the survival of auditory neurons is not uniform along the length of the cochlea for individual CI subjects with possibly sections of complete loss denoted as ‘dead regions’ (Won et al., 2015). Therefore, the number of auditory nerve cells needs to be individually determined for subjects with ‘dead regions’. It was shown that decreasing auditory nerve cell number led to increase in SRTs (speech reception threshold) for the modeled speech intelligibility (Fredelake and Hohmann, 2012). Thus, it would be interesting to look at model simulations for CI subjects with ‘dead regions’.

The NSIM index measure was used in this study to compare our phenomenological model with the auditory periphery model of Zilany et al. (2009, 2014). NSIM values calculated with the Hines and Harte (2010, 2012) and the Wirtzfeld et al. (2017a,b) scaling methods were consistent with the CI subjects’ performance in the MCI test. However, NSIM values from the Wirtzfeld et al. (2017a,b) method were smaller than the Hines and Harte (2010, 2012). A possible explanation is that in the Hines and Harte (2010, 2012) method the local NSIM regions with no spike activity would have an NSIM of unity while the local NSIM regions with spike activity would have an NSIM value less than unity. Therefore, averaging the local NSIM regions led to the bigger values for the NSIM index measure (Wirtzfeld, 2016). Further investigations with more CI subjects should be conducted to explore the possible benefits of one scaling method over the other one.

5. Conclusion

A phenomenological model of ANFs responses to the CI stimulation was developed that can explain the performances of CI recipients on a melodic contour identification task with two alternative speech processor filterbanks. The model responses were in good agreement with the MCI experiment results and in these case studies the electrodogram was not able to predict the results correctly. The model was validated for the CI electrical stimulation patterns generated with different clinical maps and can be used to evaluate CI sound coding strategies.

Author contributions

Sonia Tabibi: Conceptualization, methodology, software, validation, formal analysis, investigation, data curation, writing – original draft, visualization. Jason Boulet: Methodology, software, validation. Norbert Dillier: Resources, writing – review & editing, supervision, funding acquisition. Ian C. Bruce: Conceptualization, software, resources, data curation, writing – review & editing, supervision, project administration.

Declaration of competing interest

The authors report no declarations of interest.

Acknowledgments

Funding: This work was supported by the people Programme (Marie Curie Actions) of the European Union’s Seventh Framework Programme FP7/2007–2013 [grant numberPITN-GA-2012-317521]. Funding for the completion of first author’s PhD thesis is provided by the University of Zurich and the Truus und Gerrit van Riemsdijk Foundation. J. Boulet and I. Bruce were supported by NSERC Discovery Grant261736awarded to I. Bruce.

The authors would like to thank Dr. Henry Luetcke from Scientific IT Services of ETH Zurich for his help with running the model simulation on the Euler cluster.

Appendix A. General structure of single-fiber model

The basis of the auditory single-fiber model was the Bruce et al. (1999a,c) stochastic model. In this model, the membrane potential fluctuations were characterized by adding a noise potential V_σ to the model which had a Gaussian amplitude distribution and a $1/f$ spectrum (Verveen and Derksen, 1968). When the stimulus potential V_{stim} crossed the ‘noisy’ threshold potential $V_{\text{thr}} + V_\sigma$, an action potential was generated. Due to the uncertainty about the exact nature of the noise, the standard deviation of the noise potential remained proportional to the resting threshold during the refractory period (Bruce et al., 1999c). Therefore, the relative spread for the single pulse response (RS_{SP}) which determines the neuron’s dynamic range was defined as the standard deviation of the noise (σ) divided by the threshold for the single pulse response (θ_{SP});

$$\text{RS}_{\text{SP}} = \sigma/\theta_{\text{SP}} \tag{A.1}$$

Table A1
Summary of parameters for the phenomenological single-fiber model. Adapted from Boulet (2016).

Parameter	Symbol	Value	Reference
Single pulse response			
Threshold current	θ_{SP}	50 pA	Negm and Bruce (2014)
Relative spread	RS_{SP}	0.05	Negm and Bruce (2014)
Threshold potential	$V_{\theta,0}$	30 mV	Negm and Bruce (2014)
Membrane			
Resistance	R_{mem}	1.9535 GΩ	Negm and Bruce (2014)
Capacitance	C_{mem}	0.0714 pF	Negm and Bruce (2014)
Time constant	τ_{mem}	0.1395 ms	Negm and Bruce (2014)
Refractoriness			
Threshold absolute refractory period	t_{abs}	0.332 ms	Miller et al. (2001)
Threshold relative refractory period	$\tau_{\theta,r}$	0.411 ms	Miller et al. (2001)
Relative spread refractory time constant	$\tau_{RS,r}$	0.2 ms	Miller et al. (2001)
Spike rate adaptation (SRA)			
Threshold SRA increment	$\rho_{\theta,s}$	0.04	Nourski et al. (2006)
Threshold SRA time constant	$\tau_{\theta,s}$	50 ms	Nourski et al. (2006)
Relative spread SRA increment	$\rho_{RS,s}$	0.04	Text
Relative spread SRA time constant	$\tau_{RS,s}$	50 ms	Text
Facilitation			
Threshold time constant	$\tau_{\theta,f}$	0.5 ms	Dynes (1996)
Threshold strength	$a_{\theta,f}$	$-0.15\ ms^{-1}$	Dynes (1996)
Relative spread time constant	$\tau_{RS,f}$	0.3 ms	Dynes (1996)
Relative spread strength	$a_{RS,f}$	$0.75\ ms^{-1}$	Dynes (1996)
Accommodation			
Threshold time constant (quick)	τ_{θ,a_q}	1.5 ms	Dynes (1996)
Threshold strength (quick)	a_{θ,a_q}	$0.5\ ms^{-1}$	Dynes (1996)
Relative spread time constant (quick)	τ_{RS,a_q}	0.3 ms	Dynes (1996)
Relative spread strength (quick)	a_{RS,a_q}	$0.75\ ms^{-1}$	Dynes (1996)
Threshold time constant (slow)	τ_{θ,a_s}	50 ms	Text
Threshold strength (slow)	a_{θ,a_s}	$0.01\ ms^{-1}$	Text
Relative spread time constant (slow)	τ_{RS,a_s}	50 ms	Text
Relative spread strength (slow)	a_{RS,a_s}	$0\ ms^{-1}$	Text

The mean RS for the population of ANFs was set to 0.05 with a Gaussian distribution, SD of 0.04 and a minimum of 0 (Negm and Bruce, 2014; van Gendt et al., 2016) and the membrane capacitance (C_{mem}) and resistance (R_{mem}) were set to 0.0714 pF and 1.9535 GΩ (Negm and Bruce, 2014). The temporal phenomena parameters were set the same as in the Boulet (2016) model which are summarized in Table Table A1.

Appendix B. Effect of temporal phenomena in the single-fiber model

Refractoriness limits the maximum firing rate in cases when the time between consecutive pulses is less than the absolute refractory period. Therefore, absolute refractoriness sets the upper limit on both the onset spike rate and final spike rate. This means that long-term reductions in ANF excitability cannot be due to refractoriness. In addition, active facilitation in our model cannot accumulate beyond two pulses. Thus, accommodation and spike rate adaptation are the only phenomena which could produce spike rate decrements over the time scales of 10–100 ms in our model. This is shown in Fig. A1 by turning on or off accommodation and spike rate adaptation and both refractoriness and facilitation are on to limit their effects.

In Fig. A1 with stimulation rates of 5,000 pulses/s and 10,000 pulses/s, the model version with accommodation turned on and spike rate adaptation turned off (red line) shows a decrease in response rate compared to the case with both accommodation and spike rate adaptation turned off (black line). This shows that with increasing the pulse rate, accommodation accumulates greater over time, resulting in reduced response rate. However, at high current levels and high pulse rates, spike rate adaptation causes decrements in ANF excitability (blue line compared to the red line in bottom graph of 5,000 pulses/s and both middle and bottom graphs of 10,000 pulses/s). Both accommodation and spike rate adaptation together (green line) decrease ANF excitability towards non-spiking activity with increasing pulse rates.

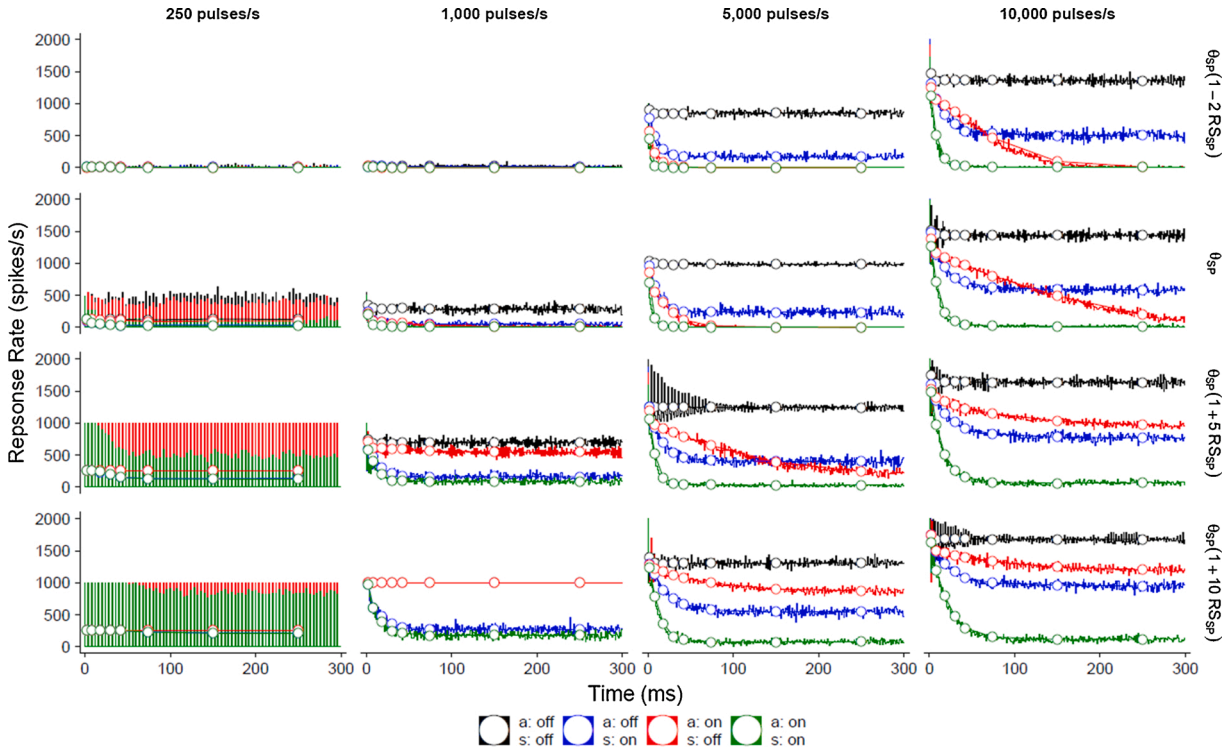

Fig. A1. Effect of temporal phenomena on response rates to pulse train stimulation with 250, 1000, 5000, and 10,000 pulses/s rates and $\theta_{SP}(1+u\mathrm{RS}_{\mathrm{SP}})$ current levels, where $u=-2$, 0, 5, 10, θ_{SP} is the threshold and $\mathrm{RS}_{\mathrm{SP}}$ is the relative spread for the single pulse response. Response rates were calculated with two sets of bins: 1 ms (thin lines) and increasing width (by binning spike counts with the increasingly wider intervals; 0–4, 4–12, 12–24, 24–36, 36–48, 48–100, 100–200, and 200–300 ms; Zhang et al., 2007) which is shown by thick lines with white dots. In all model versions, refractoriness and facilitation are turned on; only accommodation and spike rate adaptation are varied which produce four model versions with four colors.

References

Abbas, P.J., Brown, C.J., Shallop, J.K., Firszt, J.B., Hughes, M.L., Hong, S.H., Staller, S.J., 1999. Summary of results using the Nucleus CI24M implant to record the electrically evoked compound action potential. Ear Hear. 20, 45–59.

Abbas, P.J., Hughes, M.L., Brown, C.J., Miller, C.A., South, H., 2004. Channel interaction in cochlear implant users evaluated using the electrically evoked compound action potential. Audiol. Neurotol. 9, 203–213. https://doi.org/10.1159/000078390.

Botros, A., Psarros, C., 2010. Neural response telemetry reconsidered: II. The influence of neural population on the ECAP recovery function and refractoriness. Ear Hear. 31, 380–391. https://doi.org/10.1097/AUD.0b013e3181cb41aa.

Boulet, J., 2016. Biophysical and Phenomenological Models of Cochlear Implant Stimulation (Ph.D. thesis). McMaster University. http://hdl.handle.net/11375/20466.

Boulet, J., Bruce, I.C., 2017. Predictions of the contribution of HCN half-maximal activation potential heterogeneity to variability in intrinsic adaptation of spiral ganglion neurons. J. Assoc. Res. Otolaryngol. 18, 301–322. https://doi.org/10.1007/s10162-016-0605-5.

Boulet, J., White, M., Bruce, I.C., 2016. Temporal considerations for stimulating spiral ganglion neurons with cochlear implants. J. Assoc. Res. Otolaryngol. 17, 1–17. https://doi.org/10.1007/s10162-015-0545-5.

Bruce, I.C., 2017. A physiologically based predictors of speech intelligibility. Acoust. Soc. Am. 13, 28–35.

Bruce, I.C., Irlicht, L.S., White, M.W., O'Leary, S.J., Dynes, S., Javel, E., Clark, G.M., 1999a. A stochastic model of the electrically stimulated auditory nerve: pulse-train response. IEEE Trans. Biomed. Eng. 46, 630–637. https://doi.org/10.1109/10.764938.

Bruce, I.C., White, M.W., Irlicht, L.S., O'Leary, S.J., Clark, G.M., 1999b. The effects of stochastic neural activity in a model predicting intensity perception with cochlear implants: low-rate stimulation. IEEE Trans. Biomed. Eng. 46, 1393–1404. https://doi.org/10.1109/10.804567.

Bruce, I.C., White, M.W., Irlicht, L.S., O'Leary, S.J., Dynes, S., Javel, E., Clark, G.M., 1999c. A stochastic model of the electrically stimulated auditory nerve: single-pulse response. IEEE Trans. Biomed. Eng. 46, 617–629. https://doi.org/10.1109/10.764938.

Cartee, L.A., van den Honert, C., Finley, C.C., Miller, R.L., 2000. Evaluation of a model of the cochlear neural membrane. I. Physiological measurement of membrane characteristics in response to intrameatal electrical stimulation. Hear. Res. 146, 143–152. https://doi.org/10.1016/S0378-5955(00)00109-X.

Cohen, L.T., 2009a. Practical model description of peripheral neural excitation in cochlear implant recipients: 1. Growth of loudness and ECAP amplitude with current. Hear. Res. 247, 87–99. https://doi.org/10.1016/j.heares.2008.11.003.

Cohen, L.T., 2009b. Practical model description of peripheral neural excitation in cochlear implant recipients: 2. Spread of the effective stimulation field (ESF), from ECAP and FEA. Hear. Res. 247, 100–111. https://doi.org/10.1016/j.heares.2008.11.004.

Cohen, L.T., 2009c. Practical model description of peripheral neural excitation in cochlear implant recipients: 5. Refractory recovery and facilitation. Hear. Res. 248, 1–14. https://doi.org/10.1016/j.heares.2008.11.007.

Cohen, L.T., Richardson, L.M., Saunders, E., Cowan, R.S., 2003. Spatial spread of neural excitation in cochlear implant recipients: comparison of improved ECAP method and psychophysical forward masking. Hear. Res. 179, 72–87. https://doi.org/10.1016/S0378-5955(03)00096-0.

Cohen, L.T., Saunders, E., Richardson, L.M., 2004. Spatial spread of neural excitation: comparison of compound action potential and forward-masking data in cochlear implant recipients. Int. J. Audiol. 43, 346–355. https://doi.org/10.1080/14992020400050044.

Dynes, S.B.C., 1996. Discharge Characteristics of Auditory Nerve Fibers for Pulsatile Electrical Stimuli (Ph.D. thesis). Massachusetts Institute of Technology.

Fredelake, S., Hohmann, V., 2012. Factors affecting predicted speech intelligibility with cochlear implants in an auditory model for electrical stimulation. Hear. Res. 287, 76–90. https://doi.org/10.1016/j.heares.2012.03.005.

Galvin III, J.J., Fu, Q.J., Nogaki, G., 2007. Melodic contour identification by cochlear implant listeners. Ear Hear. 28, 302. https://doi.org/10.1097/01.aud.0000261689.35445.20.

van Gendt, M., Briaire, J., Kalkman, R., Frijns, J., 2016. A fast, stochastic, and adaptive model of auditory nerve responses to cochlear implant stimulation. Hear. Res. 341, 130–143. https://doi.org/10.1016/j.heares.2016.08.011.

Grayden, D.B., Burkitt, A.N., Kenny, O.P., Clarey, J.C., Paolini, A.G., Clark, G.M., 2004. A cochlear implant speech processing strategy based on an auditory model. Proceedings of the 2004 Intelligent Sensors, Sensor Networks and Information Processing Conference, 2004 491–496. https://doi.org/10.1109/ISSNIP.2004.1417510.

Greenwood, D.D., 1990. A cochlear frequency-position function for several species – 29 years later. J. Acoust. Soc. Am. 87, 2592–2605. https://doi.org/10.1121/1.399052.

Hamacher, V., 2004. Signalverarbeitungsmodelle des elektrisch stimulierten Gehörs. Mainz.

Heffer, L.F., Sly, D.J., Fallon, J.B., White, M.W., Shepherd, R.K., O'Leary, S.J., 2010. Examining the auditory nerve fiber response to high rate cochlear implant stimulation: chronic sensorineural hearing loss and facilitation. J. Neurophysiol. 104, 3124–3135. https://doi.org/10.1152/jn.00500.2010.

Hey, M., Müller-Deile, J., Hessel, H., Killian, M., 2017. Facilitation and refractoriness of the electrically evoked compound action potential. Hear. Res. 355, 14–22. https://doi.org/10.1016/j.heares.2017.09.001.

Hines, A., Harte, N., 2010. Speech intelligibility from image processing. Speech Commun. 52, 736–752. https://doi.org/10.1016/j.specom.2010.04.006.
Hines, A., Harte, N., 2012. Speech intelligibility prediction using a neurogram similarity index measure. Speech Commun. 54, 306–320. https://doi.org/10.1016/j.specom.2011.09.004.
Hodgkin, A.L., Huxley, A.F., 1952. A quantitative description of membrane current and its application to conduction and excitation in nerve. J. Physiol. 117, 500–544. https://doi.org/10.1113/jphysiol.1952.sp004764.
Hughes, M.L., Abbas, P.J., 2006. The relation between electrophysiologic channel interaction and electrode pitch ranking in cochlear implant recipients. J. Acoust. Soc. Am. 119, 1527–1537. https://doi.org/10.1121/1.2163273.
Hughes, M.L., Castioni, E.E., Goehring, J.L., Baudhuin, J.L., 2012. Temporal response properties of the auditory nerve: data from human cochlear-implant recipients. Hear. Res. 285, 46–57. https://doi.org/10.1016/j.heares.2012.01.010.
Hughes, M.L., Laurello, S.A., 2017. Effect of stimulus level on the temporal response properties of the auditory nerve in cochlear implants. Hear. Res. https://doi.org/10.1016/j.heares.2017.06.004.
Hughes, M.L., Stille, L.J., 2010. Effect of stimulus and recording parameters on spatial spread of excitation and masking patterns obtained with the electrically evoked compound action potential in cochlear implants. Ear Hear. 31, 679. https://doi.org/10.1097/AUD.0b013e3181e1d19e.
Imennov, N.S., Rubinstein, J.T., 2009. Stochastic population model for electrical stimulation of the auditory nerve. IEEE Trans. Biomed. Eng. 56, 2493–2501. https://doi.org/10.1109/TBME.2009.2016667.
Irwin, C., 2006. NIC v2 Software Interface Specification E11318RD (Technical Report). Cochlear Ltd, Lane Cove, NSW, Australia.
Jeng, F.C., Abbas, P.J., Hu, N., Miller, C.A., Nourski, K.V., Robinson, B.K., 2009. Effects of temporal properties on compound action potentials in response to amplitude-modulated electric pulse trains in guinea pigs. Hear. Res. 247, 47–59. https://doi.org/10.1016/j.heares.2008.10.007.
Kang, S., Chwodhury, T., Moon, I.J., Hong, S.H., Yang, H., Won, J.H., Woo, J., 2015. Effects of electrode position on spatiotemporal auditory nerve fiber responses: a 3D computational model study. Comput. Math. Methods Med. 2015 https://doi.org/10.1155/2015/934382.
Karg, S., Lackner, C., Hemmert, W., 2013. Temporal interaction in electrical hearing elucidates auditory nerve dynamics in humans. Hear. Res. 299, 10–18. https://doi.org/10.1016/j.heares.2013.01.015.
Lai, W., Dillier, N., 2009. Neural adaptation and the ECAP response threshold: a pilot study. Cochlear Implants Int. 10, 63–67. https://doi.org/10.1179/cim.2009.10.Supplement-1.63.
Lai, W., Dillier, N., Killian, M., 2018. A neural excitability based coding strategy for cochlear implants. J. Biomed. Sci. Eng. 11, 159. https://doi.org/10.4236/jbise.2018.117014.
Lai, W.K., Dillier, N., 2000. A simple two-component model of the electrically evoked compound action potential in the human cochlea. Audiol. Neurotol. 5, 333–345. https://doi.org/10.1159/000013899.
Lai, W.K., Müller-Deile, J., Dillier, N., Almqvist, B., Stecker, M., Frohne, C., Von Wallenberg, E., 2002. Measurement of the electrically evoked compound action potential via a neural response telemetry system. Ann. Otol. Rhinol. Laryngol. 111, 407–414. https://doi.org/10.1177/000348940211100505.
Laneau, J., Wouters, J., Moonen, M., 2006. Improved music perception with explicit pitch coding in cochlear implants. Audiol. Neurotol. 11, 38–52. https://doi.org/10.1159/000088853.
Liu, W., Edin, F., Atturo, F., Rieger, G., Löwenheim, H., Senn, P., Blumer, M., Schrott-Fischer, A., Rask-Andersen, H., Glueckert, R., 2015. The pre- and post-somatic segments of the human type I spiral ganglion neurons – structural and functional considerations related to cochlear implantation. Neuroscience 284, 470–482. https://doi.org/10.1016/j.neuroscience.2014.09.059.
Miller, C.A., Abbas, P.J., Robinson, B.K., 2001. Response properties of the refractory auditory nerve fiber. JARO J. Assoc. Res. Otolaryngol. 2, 216–232. https://doi.org/10.1007/s101620010083.
Miller, C.A., Abbas, P.J., Robinson, B.K., Rubinstein, J.T., Matsuoka, A.J., 1999. Electrically evoked single-fiber action potentials from cat: responses to monopolar, monophasic stimulation. Hear. Res. 130, 197–218. https://doi.org/10.1016/S0378-5955(98)00046-X.
Miller, C.A., Hu, N., Zhang, F., Robinson, B.K., Abbas, P.J., 2008. Changes across time in the temporal responses of auditory nerve fibers stimulated by electric pulse trains. J. Assoc. Res. Otolaryngol. 9, 122–137. https://doi.org/10.1007/s10162-007-0108-5.
Mino, H., Rubinstein, J.T., Miller, C.A., Abbas, P.J., 2004. Effects of electrode-to-fiber distance on temporal neural response with electrical stimulation. IEEE Trans. Biomed. Eng. 51, 13–20. https://doi.org/10.1109/TBME.2003.820383.
Negm, M.H., Bruce, I.C., 2014. The effects of HCN and KLT ion channels on adaptation and refractoriness in a stochastic auditory nerve model. IEEE Trans. Biomed. Eng. 61, 2749–2759. https://doi.org/10.1109/TBME.2014.2327055.
Nie, K., Stickney, G., Zeng, F.G., 2005. Encoding frequency modulation to improve cochlear implant performance in noise. IEEE Trans. Biomed. Eng. 52, 64–73. https://doi.org/10.1109/TBME.2004.839799.
Nogueira, W., Büchner, A., Lenarz, T., Edler, B., 2005. A psychoacoustic NofM-type speech coding strategy for cochlear implants. EURASIP J. Appl. Signal Process. 2005, 3044–3059. https://doi.org/10.1155/ASP.2005.3044.
Nourski, K., Abbas, P., Miller, C., Robinson, B., Jeng, F., 2006. Effects of Remaining Hair Cells on Cochlear Implant Function. 15th Quarterly Progress Report. NIH Contract.
O'Brien, G.E., Rubinstein, J.T., 2016. The development of biophysical models of the electrically stimulated auditory nerve: single-node and cable models. Network: Comput. Neural Syst. 27, 135–156. https://doi.org/10.3109/0954898X.2016.1162338.
Rattay, F., 1999. The basic mechanism for the electrical stimulation of the nervous system. Neuroscience 89, 335–346. https://doi.org/10.1016/S0306-4522(98)00330-3.
Seeber, B.U., Bruce, I.C., 2016. The history and future of neural modeling for cochlear implants. Network: Comput. Neural Syst. 27, 53–66. https://doi.org/10.1080/0954898X.2016.1223365.
Sit, J.J., Simonson, A.M., Oxenham, A.J., Faltys, M.A., Sarpeshkar, R., 2007. A low-power asynchronous interleaved sampling algorithm for cochlear implants that encodes envelope and phase information. IEEE Trans. Biomed. Eng. 54, 138–149. https://doi.org/10.1109/TBME.2006.883819.
Spoendlin, H., Schrott, A., 1989. Analysis of the human auditory nerve. Hear. Res. 43, 25–38. https://doi.org/10.1016/0378-5955(89)90056-7.
Tabibi, S., Kegel, A., Lai, W.K., Bruce, I.C., Dillier, N., 2019. Measuring temporal response properties of auditory nerve fibers in cochlear implant recipients. Hear. Res. 380, 187–196. https://doi.org/10.1016/j.heares.2019.07.004.
Tabibi, S., Kegel, A., Lai, W.K., Dillier, N., 2017. Investigating the use of a Gammatone filterbank for a cochlear implant coding strategy. J. Neurosci. Methods 277, 63–74. https://doi.org/10.1016/j.jneumeth.2016.12.004.
Tabibi, S., Kegel, A., Lai, W.K., Dillier, N., 2020. A bio-inspired coding (BIC) strategy for cochlear implants. Hear. Res. 388, 107885. https://doi.org/10.1016/j.heares.2020.107885.
Takanen, M., Bruce, I.C., Seeber, B.U., 2016. Phenomenological modelling of electrically stimulated auditory nerve fibers: a review. Network: Comput. Neural Syst. 27, 157–185. https://doi.org/10.1080/0954898X.2016.1219412.
Tykocinski, M., Saunders, E., Cohen, L.T., Treaba, C., Briggs, R.J., Gibson, P., Clark, G.M., Cowan, R.S., 2001. The contour electrode array: safety study and initial patient trials of a new perimodiolar design. Otol. Neurotol. 22, 33–41.
Undurraga, J.A., Carlyon, R.P., Macherey, O., Wouters, J., Van Wieringen, A., 2012. Spread of excitation varies for different electrical pulse shapes and stimulation modes in cochlear implants. Hear. Res. 290, 21–36. https://doi.org/10.1016/j.heares.2012.05.003.
van der Beek, F.B., Briaire, J.J., Frijns, J.H., 2012. Effects of parameter manipulations on spread of excitation measured with electrically-evoked compound action potentials. Int. J. Audiol. 51, 465–474. https://doi.org/10.3109/14992027.2011.653446.
Vandali, A.E., van Hoesel, R.J., 2011. Development of a temporal fundamental frequency coding strategy for cochlear implants. J. Acoust. Soc. Am. 129, 4023–4036. https://doi.org/10.1121/1.3573988.
Verveen, A., 1962. Axon diameter and fluctuation in excitability. Acta Morphol. Neerl. Scand. 5, 79–85.
Verveen, A., Derksen, H., 1968. Fluctuation phenomena in nerve membrane. Proc. IEEE 56, 906–916. https://doi.org/10.1109/PROC.1968.6443.
Wang, Z., Bovik, A.C., Sheikh, H.R., Simoncelli, E.P., et al., 2004. Image quality assessment: from error visibility to structural similarity. IEEE Trans. Image Process. 13, 600–612. https://doi.org/10.1109/TIP.2003.819861.
Wilson, B.S., Dorman, M.F., 2008. Cochlear implants: a remarkable past and a brilliant future. Hear. Res. 242, 3–21. https://doi.org/10.1016/j.heares.2008.06.005.
Wilson, B.S., Schatzer, R., Lopez-Poveda, E.A., Sun, X., Lawson, D.T., Wolford, R.D., 2005. Two new directions in speech processor design for cochlear implants. Ear Hear. 26, 73S–81S.
Wirtzfeld, M.R., 2016. Predicting Speech Intelligibility and Quality from Model Auditory Nerve Fiber Mean-Rate and Spike-Timing Activity (Ph.D. thesis). McMaster University.
Wirtzfeld, M.R., Ibrahim, R.A., Bruce, I.C., 2017a. Predictions of speech chimaera intelligibility using auditory nerve mean-rate and spike-timing neural cues. J. Assoc. Res. Otolaryngol. 18, 687–710. https://doi.org/10.1007/s10162-017-0627-7.
Wirtzfeld, M.R., Pourmand, N., Parsa, V., Bruce, I.C., 2017b. Predicting the quality of enhanced wideband speech with a cochlear model. J. Acoust. Soc. Am. 142, EL319–EL325. https://doi.org/10.1121/1.5003785.
Won, J.H., Jones, G.L., Moon, I.J., Rubinstein, J.T., 2015. Spectral and temporal analysis of simulated dead regions in cochlear implants. J. Assoc. Res. Otolaryngol. 16, 285–307. https://doi.org/10.1007/s10162-014-0502-8.
Woo, J., Miller, C.A., Abbas, P.J., 2010. The dependence of auditory nerve rate adaptation on electric stimulus parameters, electrode position, and fiber diameter: a computer model study. J. Assoc. Res. Otolaryngol. 11, 283–296. https://doi.org/10.1007/s10162-009-0199-2.
Zhang, F., Benson, C., Murphy, D., Boian, M., Scott, M., Keith, R., Xiang, J., Abbas, P., 2013. Neural adaptation and behavioral measures of temporal processing and speech perception in cochlear implant recipients. PLoS One 8, e84631. https://doi.org/10.1371/journal.pone.0084631.
Zhang, F., Miller, C.A., Robinson, B.K., Abbas, P.J., Hu, N., 2007. Changes across time in spike rate and spike amplitude of auditory nerve fibers stimulated by electric pulse trains. J. Assoc. Res. Otolaryngol. 8, 356–372. https://doi.org/10.1007/s10162-007-0086-7.
Zilany, M.S., Bruce, I.C., Carney, L.H., 2014. Updated parameters and expanded simulation options for a model of the auditory periphery. J. Acoust. Soc. Am. 135, 283–286. https://doi.org/10.1121/1.4837815.
Zilany, M.S., Bruce, I.C., Nelson, P.C., Carney, L.H., 2009. A phenomenological model of the synapse between the inner hair cell and auditory nerve: long-term adaptation with power-law dynamics. J. Acoust. Soc. Am. 126, 2390–2412. https://doi.org/10.1121/1.3238250.